Geophysical Journal International

Geophys. J. Int. (2016) **207,** 244–258
Advance Access publication 2016 July 25
GJI Seismology

doi: 10.1093/gji/ggw271

Anisotropy from SKS splitting across the Pacific-North America plate boundary offshore southern California

Joseph Ramsay,[1] Monica D. Kohler,[2] Paul M. Davis,[1] Xinguo Wang,[3,4] William Holt[4] and Dayanthie S. Weeraratne[5]

[1]*Department of Earth and Space Sciences, University of California Los Angeles, Los Angeles, CA* 90095-1596, *USA*
[2]*Department of Mechanical and Civil Engineering, California Institute of Technology, Pasadena, CA* 91125, *USA. E-mail: kohler@caltech.edu*
[3]*Key Laboratory of Continental Collision and Plateau Uplift, Institute of Tibetan Plateau Research, Chinese Academy of Sciences, Beijing, China*
[4]*Department of Geosciences, Stony Brook University, Stony Brook, NY* 11794-2100, *USA*
[5]*Department of Geological Sciences, California State University Northridge, Northridge, CA* 91330-8266, *USA*

Accepted 2016 July 19. Received 2016 July 18; in original form 2015 October 19

SUMMARY

SKS arrivals from ocean bottom seismometer (OBS) data from an offshore southern California deployment are analysed for shear wave splitting. The project involved 34 OBSs deployed for 12 months in a region extending up to 500 km west of the coastline into the oceanic Pacific plate. The measurement process consisted of removing the effects of anisotropy using a range of values for splitting fast directions and delay times to minimize energy along the transverse seismometer axis. Computed splitting parameters are unexpectedly similar to onland parameters, exhibiting WSW–ENE fast polarization directions and delays between 0.8 and 1.8 s, even for oceanic plate sites. This is the first SKS splitting study to extend across the entire boundary between the North America and Pacific plates, into the oceanic part of the Pacific plate. The splitting results show that the fast direction of anisotropy on the Pacific plate does not align with absolute plate motion (APM), and they extend the trend of anisotropy in southern California an additional 500 km west, well onto the oceanic Pacific plate. We model the finite strain and anisotropy within the asthenosphere associated with density–buoyancy driven mantle flow and the effects of APM. In the absence of plate motion effects, such buoyancy driven mantle flow would be NE-directed beneath the Pacific plate observations. The best-fit patterns of mantle flow are inferred from the tomography-based models that show primary influences from foundering higher-density zones associated with the history of subduction beneath North America. The new offshore SKS measurements, when combined with measurements onshore within the plate boundary zone, indicate that dramatic lateral variations in density-driven upper-mantle flow are required from offshore California into the plate boundary zone in California and western Basin and Range.

Key words: Body waves; Seismic anisotropy; Continental margins: transform; Dynamics of lithosphere and mantle; Pacific Ocean.

INTRODUCTION

Many mantle flow models depend on constraints provided by anisotropy data from either body waves or surface waves; however, the depth dependence of those measurements is not well-resolved for the entire Pacific-North America plate boundary. This has led to uncertainty about what the seismic velocity and anisotropy measurements indicate about current versus ancient plate motion and mantle flow directions. In onshore southern California, the majority of SKS splitting measurements show fast polarization directions that are approximately EW across a wide zone in southern California (e.g. Savage *et al*. 1990; Silver & Savage 1994; Liu *et al*. 1995; Özalaybey & Savage 1995; Polet & Kanamori 2002; Kosarian *et al*. 2011; Monteiller & Chevrot 2011), even west of the San Andreas fault where recent geodetic (GPS) monitoring shows relative Pacific plate surface movement to the northwest.

Surface wave azimuthal anisotropy averaged over the area covered by the permanent Southern California Seismic Network varies uniformly in this unusually complex region, with a uniform EW fast direction for periods between 20–40 s that changes slightly to NW–SE at longer periods up to 110 s (Yang & Forsyth 2006). The magnitude of peak-to-peak anisotropy is 1.7 per cent at periods below 40 s, decreasing to 1 per cent for longer periods, predicting a shear wave splitting measurement of only 0.25–0.4 s in the

lithosphere (assuming a 90 km lithospheric depth). This implies that the remaining 1.1 s observed in splitting measurements occurs at sublithospheric depths as deep as ∼300 km (Yang & Forsyth 2006). In the oceanic mantle, we can expect lithospheric anisotropy to be stronger (up to ∼3.5 per cent peak-to-peak) than in continental lithosphere (Weeraratne *et al*. 2007). However, the contribution from the sublithospheric mantle may be similar below both oceanic and continental plates if mantle flow is predominantly large scale in this region. Alternatively, other studies maintain that a model of two or more layers may explain the SKS parameters (Özalaybey & Savage 1995) without the need to ascribe to such a deep anisotropic mantle layer.

Almost half the diffuse, transpressional, 500 km wide Pacific-North America plate boundary in southern California lies offshore. The impingement of the East Pacific Rise with the western boundary of the North America plate marked the end of Farallon plate subduction 37–30 Myr (Atwater 1970; Engebretson *et al*. 1985; Wright 1991). After a long period of Pacific plate subduction along the entire western margin of the North America plate, the East Pacific spreading centre began to approach this western continental boundary. Upon subduction of the spreading centre, fracture and breakup of the Pacific plate at the offshore margin ensued, beginning with the breakup and sudden rotation of the Monterey microplate 29 Myr (Atwater 1989). The Borderland, Los Angeles region and Mojave Desert subsequently underwent crustal extension and rifting that began 24–18 Myr (Dokka 1989; Tennyson 1989; Wright 1991), accommodated by normal faulting (Crouch & Suppe 1993). Seafloor isochron maps indicate that fracture and formation of the Arguello and Patton microplates began at isochron 6c (24 Myr) at which time the axis of the offshore Pacific-Farallon spreading centre began a steady rotation from NE–SW to NW–SE (finally consistent with San Andreas fault orientation) finishing by 18 Myr and producing arcuate-shaped fracture zones separating the microplates. The formation of the Borderland is thought to have been accompanied by ∼100° of ongoing clockwise rotation of the Transverse Ranges (Atwater 1989; Luyendyk 1991; Crouch & Suppe 1993). The formation of the left step 'big bend' in the San Andreas fault occurred 12–4 Myr ago (Crowell 1968; Atwater 1970; Stock & Hodges 1989; Wright 1991) and is the most likely source of oblique convergence in southern California (Crowell 1968). Pacific plate motion relative to North America is now oriented in a NW direction, approximately parallel to the San Andreas fault in central California. The Borderland, Los Angeles basin and Transverse Ranges are now experiencing NS contraction distributed over a broad network of offshore and onshore faults (Feigl *et al*. 1993; Shen *et al*. 1996; Walls *et al*. 1998).

Finding the correct dynamic and rheologic environment that explains anisotropy observations has implications for the nature of crustal, lithospheric and asthenospheric mantle interactions, and consequently the driving forces for continental deformation in western North America. Previous studies using seismic anisotropy and plate motion GPS data in western North America infer SW–NE plate motion over uniformly EW mantle flow (Silver & Holt 2002). An alternative study based on a compilation of plate velocity and anisotropy results suggests that toroidal flow occurs in the asthenosphere beneath much of the western U.S. to accommodate mantle flow around the subducted Juan de Fuca plate (Zandt & Humphreys 2008). Based on that study, toroidal mantle motions are predicted to occur below the Pacific-North America plate boundary in southern California. Another contrasting mantle flow model by Liu & Bird (2002) requires westward active drag of North America as well as westward drag within the plate boundary zone itself. If coupling with the lithosphere is occurring, this could be contributing significant finite strain associated with plate motions, fault loading and underlying upper-mantle flow. These different scenarios have implications for whether lithospheric deformation occurs passively with little or no mechanical coupling with the deep mantle, or actively with the primary source of plate motion coming from the deep mantle. On the regional scale, an accurate model of mantle flow needs to be consistent with the tectonic and rheologic environment in which the block rotations are either embedded in and accommodated by mantle motions, or are occurring only in crustal lithosphere and decoupled from the mantle.

One way to detect the finite strain associated with mantle flow is by measuring the effects of anisotropy on seismic waves that pass through it (Silver & Chan 1991; Silver & Holt 2002). This study examined splitting of SKS and SKKS waves recorded on an ocean bottom seismometer (OBS) network offshore southern California to infer flow in the underlying mantle. Prior to the OBS deployment, the few existing Borderland island SKS measurements (Polet & Kanamori 2002) suggested evidence for gradients in mantle flow patterns in the continental-to-oceanic Borderland tectonic transition region. However, measurements taken from island stations are not ideal because islands by nature are anomalous and may not reflect the more uniform seafloor and underlying mantle dynamics far from anomalous seafloor volcanism. Measurements offshore on the Pacific plate itself are necessary to identify oceanic plate dynamics, and to relate splitting to palaeo and recent mantle flow to test geodynamic flow models. Studying lithospheric versus asthenospheric anisotropy is particularly attractive in an oceanic setting because seafloor spreading directions provide known expectations for the fast direction of remnant anisotropy in oceanic lithosphere—something that is not true of continental lithosphere which may have had a more complex and less tractable evolutionary history.

Currently there is controversy about the origin of the anisotropy that gives rise to SKS splitting. Away from subduction zones there is a tendency for splitting to align with absolute plate motions (APMs; Montagner *et al*. 2000). This has led to the belief that SKS splitting is associated with regions shallower than ∼400 km (Becker *et al*. 2006). Previous SKS analyses in southern California by Kosarian *et al*. (2011) and Becker *et al*. (2012), however, found that SKS splitting directions align with the North America APM (WSW–ENE), including offshore where one might expect a transition to Pacific APM (Becker *et al*. 2006; Kosarian *et al*. 2011; Becker *et al*. 2012). This suggests that anisotropy is not due entirely to lithospheric drag on the asthenosphere (Kosarian *et al*. 2011). It has been proposed that the Pacific APM west of the San Andreas fault simply has not yet had time to overprint the effects of North America APM. In central California, a tendency to align with Pacific plate motion west of the San Andreas fault has been observed (Kosarian *et al*. 2011), suggesting that if APM is the cause, more finite strain has developed north of the big bend of the San Andreas fault than in southern California where the strain has been more diffuse. In that case the effective plate boundary may be offshore, beyond which splitting would align with Pacific APM. Our results show that this is not the case, and a simple APM causative model does not apply.

OCEAN BOTTOM SEISMOMETER DATA

During August 2010–September 2011, 34 OBSs were deployed in a 150 km (north–south) by 400 km (east–west) region off the coast of southern California (Fig. 1). The three-component OBSs recorded

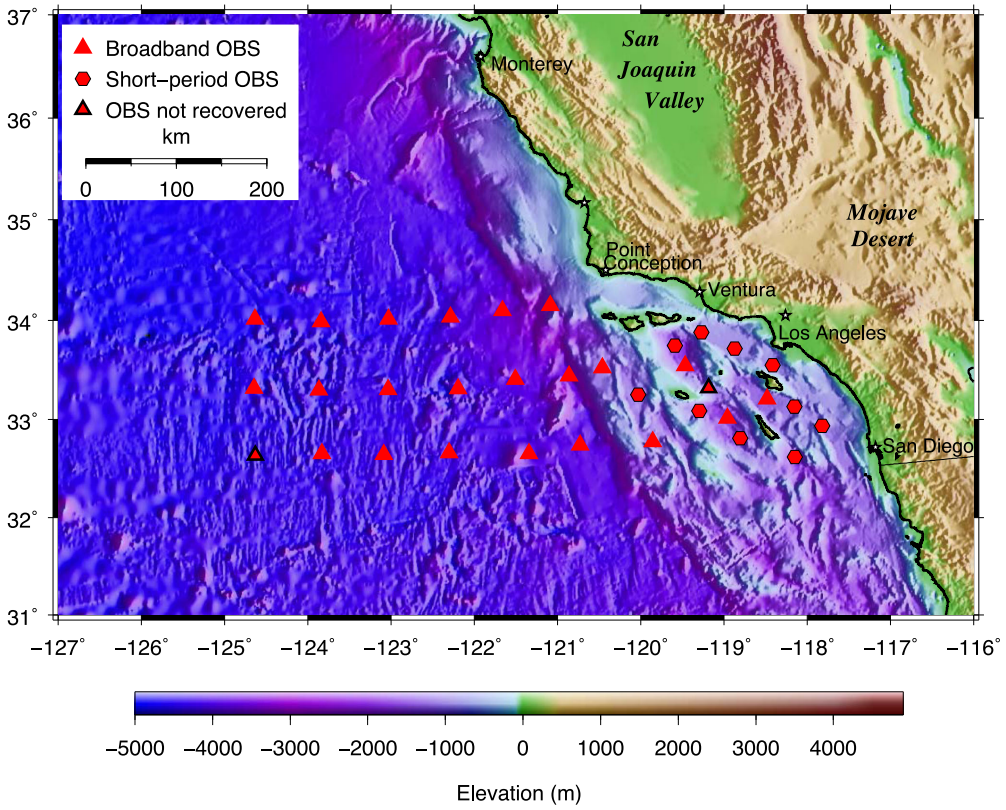

Figure 1. Offshore southern California ALBACORE 2010–2011 OBS deployment region showing array geometry. Bathymetry is ETOPO1 topography-bathymetry (Amante & Eakins 2009).

continuous waveform data for about 12 months and are part of the ALBACORE (Asthenospheric and Lithospheric Broadband Architecture from the California Offshore Region Experiment) project (Kohler *et al*. 2010, 2011). The objective of the ALBACORE project was to define the tectonic interaction across the entire Pacific-North America plate boundary by identifying the physical properties and deformation styles of the Pacific plate and the transition to continental lithosphere. The data from the OBSs are used to distinguish among contrasting upper-mantle geodynamic scenarios that predict large-scale mantle flow patterns beneath western North America. In addition to anisotropy, seismic velocities are being obtained through inversion of dispersion curve data calculated from surface waves and cross correlation of ambient noise functions (Bowden *et al*. 2016), as well as receiver function analysis (Reeves *et al*. 2015).

In the Continental Borderland region in offshore southern California, station spacing was approximately 50 km, while in the oceanic plate region spacing was approximately 75 km. Three types of OBSs were deployed: 21 long-period Nanometrics Trillium 240 sensors, 3 intermediate-period Trillium 40 sensors and 10 short-period Sercel L-28 sensors. The dataloggers on each OBS were identical, four-channel, 24-bit digitizers with solid state memory and a temperature-compensated oscillator. Waveform data were recorded continuously at 50 sps. Due to the lower-frequency bandwidth requirement for SKS arrival detection, the short-period sensors were not useful for this study. GPS time stamps were applied at the beginning and end of the 12 months of deployment, with corrections applied linearly to the data. Most time corrections were under 1 second for the entire 12-month period; the largest was ∼4 s for two stations.

Sensor horizontal orientations with respect to a reference direction are not known due to random rotation in the water column during deployment. Thus, Rayleigh wave vertical-to-horizontal amplitude ratios were analysed to determine final orientations after settling on the seafloor. Synthetic waveforms for a variety of back azimuths were correlated with the observed Rayleigh wave; the maximum positive correlation coefficient indicated the azimuth of maximum correlation (Stachnik *et al*. 2012).

SPLITTING MEASUREMENT METHOD

Anisotropy in the upper mantle causes numerous effects in seismic data: (i) shear wave splitting—the two polarizations of *S* waves arrive at different times, (ii) azimuthal anisotropy—arrival times of seismic waves at a given distance depend on the azimuth of approach and (iii) Love and Rayleigh wave dispersion values not explained by isotropic models (Anderson & Isaak 1995). In situations dominated by lattice-preferred orientation (LPO), anisotropy can exist due to a preferred orientation of anisotropic minerals and crystals (Ribe & Yu 1991). The explanations for the causes of olivine alignment have often included APM (lithospheric drag; Silver & Chan 1991) or seafloor spreading at shallow depths (Wolfe & Silver 1998; Harmon *et al*. 2004). Other studies which use long-period surface wave azimuthal anisotropy extend the analysis to several hundred kilometres depth (Beghein *et al*. 2014). The alignment of fast direction with seafloor spreading may break down for seafloor of greater age. Consequently, a two-layer model with anisotropy inherited from seafloor spreading existing in the lithosphere in addition to another layer in the direction of APM existing in the asthenosphere has been proposed (Wolfe & Silver 1998; Barruol *et al*. 2009). The relative influence of APM and seafloor spreading on the fast direction anisotropy is addressed in this study.

The effect of anisotropy can be seen in SKS arrivals which are waves that originate from the earthquake rupture area as *S* waves and travel through the mantle into the outer liquid core. Since a shear wave cannot propagate through a liquid, it becomes a *P* wave during this portion of its journey. Once this wave encounters the core–mantle boundary (CMB) on its way back up to the surface, it converts to a shear wave again. The trip throughout the core acts as a filter because it guarantees that the polarization of the emerging *S* wave is SV (radially polarized). As this wave encounters azimuthally anisotropic material it is split into fast and slow components based on the material's anisotropic orientation. The fast and slow components arrive out of phase at the surface, something that would not happen without anisotropy. These components can then be analysed bearing in mind that the initial polarization of the wave at the CMB should be almost purely SV.

Once an SKS signal is recognized in a seismogram, the phase shift between fast and slow signals δt and the fast direction φ are found by minimizing energy along the transverse axis using the method of Silver & Chan (1991). After correction for the OBS horizontal orientation, the horizontal axes of the seismogram are rotated by φ into trial fast and slow directions,

$$\begin{bmatrix} \text{fast} \\ \text{slow} \end{bmatrix} = \begin{bmatrix} \cos\varphi & \sin\varphi \\ -\sin\varphi & \cos\varphi \end{bmatrix} \begin{bmatrix} N \\ E \end{bmatrix}. \quad (1)$$

Calculation of δt between the two phases' arrival times is then used to advance the slow arrival. For this analysis FFT was performed on the slow component and was multiplied by $e^{-iw\delta t}$ where δt is a trial time shift in the attempt to remove the delay. The signals are then rotated back into geographic north–south (N) and east–west (E) axes,

$$\begin{bmatrix} N \\ E \end{bmatrix} = \begin{bmatrix} \cos(-\varphi) & \sin(-\varphi) \\ -\sin(-\varphi) & \cos(-\varphi) \end{bmatrix} \begin{bmatrix} \text{fast} \\ \text{slow} \end{bmatrix} \quad (2)$$

and finally into radial (R) and transverse (T) components

$$\begin{bmatrix} R \\ T \end{bmatrix} = \begin{bmatrix} \cos\theta & \sin\theta \\ -\sin\theta & \cos\theta \end{bmatrix} \begin{bmatrix} N \\ E \end{bmatrix}. \quad (3)$$

where θ = backazimuth $-\pi$. The energy in the transverse direction was then analysed for values of φ and δt that minimize it. Values of φ are increased by increments of 1°, between 0° and 180°, and δt is increased in increments of 0.1 s, between 0.0 s and 4.0 s. A wide range of fast directions and delay times were tested for both SKS and SKKS arrivals. Resulting contour plots of energy for each of these combinations reveal the set of parameters that minimizes energy in the transverse direction.

It has previously been shown that the splitting process separates waveforms such that the transverse component is the time derivative of the radial component (Vinnik *et al*. 1989). This is key when processing data for SKS splitting. Shear wave splitting is useful for mapping anisotropy because it is difficult to produce the observed effect of two *S* pulses of similar shape, orthogonal to each other, arriving at slightly different (<3 s) times, and with the derivative of the radial component equivalent to the tangential component, without anisotropy present somewhere along the ray path. One concern, however, is that a thin, highly anisotropic layer can produce the same delay time as a thick, weakly anisotropic layer. Independent considerations such as tectonic history can help distinguish between these two competing parameters.

SKS splitting has no depth resolution in and of itself, and therefore the depth of generation of anisotropy is uncertain since Rayleigh wave anisotropic studies generally see smaller effects than those detected by splitting (West *et al*. 2009; Kosarian *et al*. 2011; Yuan & Beghein 2013). The ALBACORE project presented a new opportunity to constrain the source of anisotropy since it is the first SKS splitting study to extend across the plate boundary between the North America and Pacific plates. Measurements across this boundary shed new light on the scale and geometry of mantle flow patterns, and associated finite strain.

In order to work with the highest signal-to-noise-ratio (SNR) SKS and SKKS phases, teleseismic earthquakes with magnitudes greater than 6.5, and epicentral distances 90° to 110° were selected. Of the 98 earthquakes that fell in this range during August 2010–September 2011, 7 showed coherent SKS or SKKS arrivals across the ALBACORE OBS network. See Table 1 for earthquakes used in this analysis. Signals from these events were bandpass filtered for frequencies between 0.06 and 0.1 Hz to obtain the best SNR. Microseismic noise limited usable frequencies to under 0.1 Hz (Wolfe & Solomon 1998). The backazimuth range of these earthquakes is illustrated by the great circle paths shown in Fig. 2.

Due to the nature of anisotropy, it is assumed that an arrival associated with a specific earthquake is usable if three criteria are met: (1) the event is seen across the ALBACORE OBS network, (2) a time delay between the radial and transverse components is observed and (3) the derivative of the radial matches the transverse component. These requirements further restricted our usable number of events. With noisy OBS data, it is necessary to ensure that we are truly analysing SKS/SKKS arrivals and not other signals such as microseisms that display similar characteristics but are incoherent between stations. These strict requirements precluded some stations from having any usable events. After all processing, reliable measurements were obtained from 11 out of the 22 recovered broadband OBSs. A sample seismogram with an acceptable signal for analysis is seen in Fig. 3 and individual shear wave splitting parameters at the OBS locations are shown in Table 2. A full set of diagnostic figures for the splitting example in Fig. 3 can be found in the Supporting Information Figs S1–S7.

Stacking methods similar to Wolfe & Solomon (1998) were also used to obtain more robust results by stacking multiple events for the same OBS station. This was especially useful due to the low number of usable events. SKS splitting methods were applied to the resulting stacked records, and results are encouragingly similar with little variation among the majority of stations, as seen in Table 3. Errors were estimated based on the F-test to find one-sigma confidence limits in the sum of squares plots of individual or stacked events. Following Silver & Chan (1991), the number of degrees of freedom was assumed to equal the total number of seconds in the data used. This gives similar numbers to the method described by Walsh *et al*. (2013).

RESULTS AND DISCUSSION

The final splitting results after stacking, including those for which there was only one event for a particular station, are illustrated in Fig. 4. They show that the fast direction of anisotropy does not align with APM as predicted by the toroidal flow model, either on the Pacific plate or in the Borderland. The results (Fig. 4 and Table 3) indicate that fast directions are oriented approximately WSW–ENE at nearly every OBS station except for one station in the Borderland which shows a more EW fast polarization direction. The one-sigma confidence limits are also plotted in Fig. 4. The stacked results also indicate delay times that are between 0.8 and 1.8 s. The larger delay times occur at Borderland stations, but there is no obvious geographic or tectonic setting pattern for either the fast polarization

Table 1. Earthquakes used in this study. BAZ: back azimuth measured clockwise from north.

Event No.	Date	Origin time	Latitude (°N)	Longitude (°E)	Depth (km)	BAZ (°)	M_w
1	09/04/2010	16:35:47	−42.52	171.83	12	223	7.0
2	09/29/2010	16:10:51	−4.91	133.71	10	275	6.2
3	09/29/2010	17:11:25	−4.96	133.76	26	275	7.0
4	01/18/2011	20:23:23	28.78	63.95	68	358	7.2
5	02/10/2011	14:41:58	4.08	123.04	525	290	6.6
6	07/11/2011	20:47:04	9.51	122.18	19	295	6.4
7	09/05/2011	17:55:11	2.96	97.89	91	309	6.7

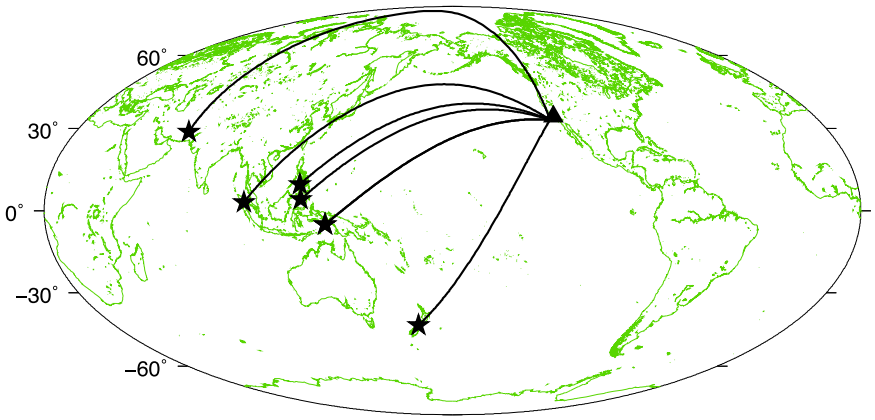

Figure 2. Great circle paths for the seven earthquakes used in this study. Note that one path lies nearly on top of another. Stars show locations of earthquakes. Triangle shows location of centre of ALBACORE OBS array.

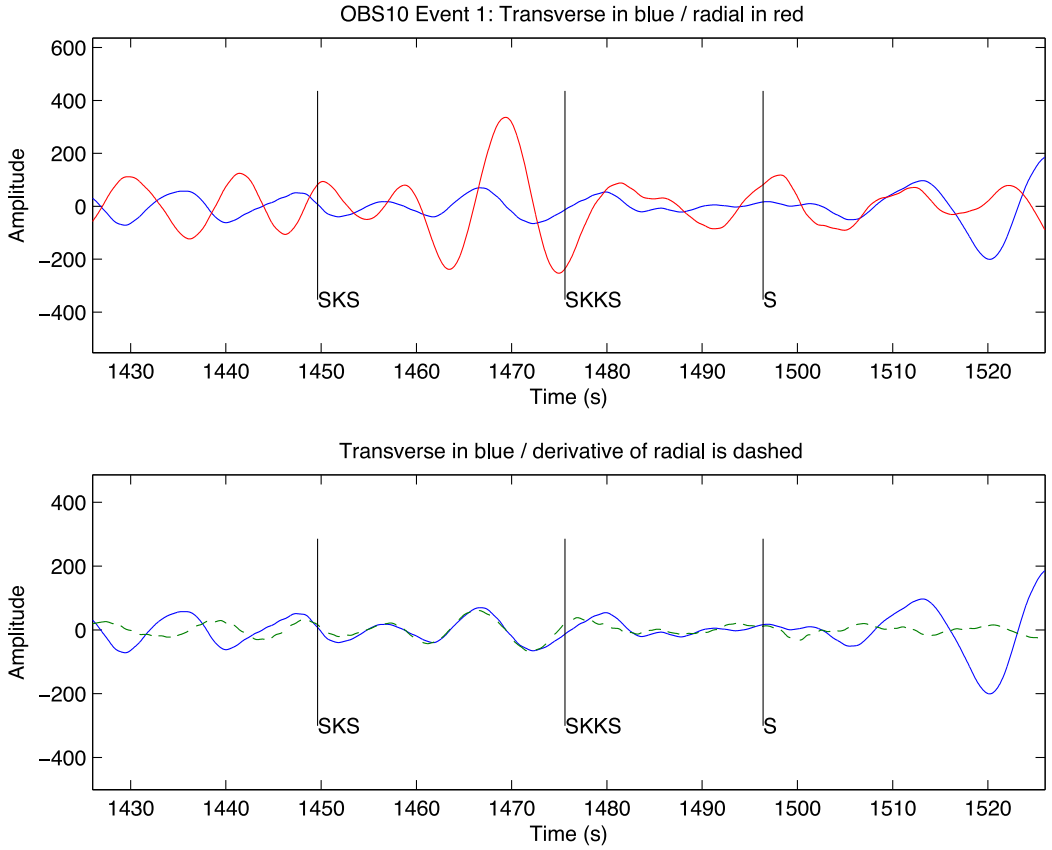

Figure 3. Sample radial and transverse seismogram pair for OBS10 illustrating an acceptable signal for analysis. Transverse component is in blue. Radial component is in red. Derivative of radial component is in dashed green.

Table 2. Individual event shear wave splitting parameters obtained at OBS locations. The direction φ of shear wave polarization is measured clockwise from north, with one-sigma error $\pm\varphi$. δt indicates splitting delay times, with one-sigma error $\pm\delta t$. See Fig. 1 for station locations.

Station	Event	φ (°)	δt (s)	$\pm\varphi$ (°)	$\pm\delta$t (s)
3	1	81	1.8	18	0.6
	6	95	2.2	5	0.4
	7	73	1.9	9	0.4
8	1	65	1.8	5	0.1
	7	99	1.6	9	0.5
10	1	66	1.1	3	0.1
11	1	73	0.8	18	0.2
	6	72	1.1	13	0.1
	7	78	1.7	9	0.2
13	1	117	2.7	2	0.4
	3	50	1.1	18	0.2
	6	89	1.8	5	0.3
	7	84	1.2	15	0.3
15	1	83	1.6	6	0.2
	5	99	3.1	3	1.0
	6	88	2.0	3	0.2
	7	84	1.7	5	0.1
18	2	68	1.1	7	0.2
19	1	75	2.1	4	0.2
	2	52	1.1	21	0.3
	3	58	1.2	23	0.3
	5	115	3.1	4	1.1
	6	62	1.2	9	0.1
	7	112	2.2	3	0.5
22	4	62	1.1	8	0.3
28	1	95	2.2	8	0.3
	5	94	1.5	3	0.2
	7	90	1.6	8	0.2
32	6	78	0.8	21	0.2

directions or the delay times. Our new measurements extend the trend of anisotropy in southern California 500 km west, well onto the Pacific plate.

The results presented here require a different explanation for the source of SKS anisotropy than simple lithospheric drag. Vertical integration between fossil seafloor spreading and APM (e.g. Wolfe & Silver 1998; Harmon *et al*. 2004) does not completely explain our observations. Seafloor magnetic anomalies in our study area indicate a shift from NS alignment in the west to NW–SE alignment near the Patton Escarpment. Fossil anisotropy is then predicted to be EW and NE–SW respectively in these sections of the seafloor. Given that our SKS splitting results align well with the various fracture zones in the region, seafloor age appears young enough (<40 Myr) to exhibit the effects of fossil spreading but too young for APM to have completely imprinted its direction on anisotropy. When more recent studies are considered, however, this explanation seems unlikely. Kosarian *et al*. (2011) found EW fast direction SKS splitting results on both sides of the big bend of the San Andreas fault, whereas their lithosphere surface wave analysis produced azimuthal anisotropy aligned with the San Andreas fault. These differences suggest that most of the SKS splitting is generated deeper than the lithosphere. If this is the case, frozen-in fossil spreading is an unlikely candidate. Furthermore, our SKS splitting measurements do not agree with predicted splitting from azimuthal anisotropy models such as Yuan & Beghein (2013) except at a depth of 200 km. This provides further evidence for a sublithospheric source of SKS anisotropy under the western side of the Pacific-North America plate boundary.

FINITE STRAIN AND MANTLE FLOW MODEL PREDICTIONS

Whereas APM cannot explain the orientation of SKS splitting measurements, the combined effects of APM with density–buoyancy driven mantle flow may be playing an important role in producing LPO within the asthenosphere. We investigate the role of density–buoyancy driven mantle flow, together with the effects of APM, in producing the SKS splitting observations. Our approach is based on the hypothesis that the anisotropic fabric (LPO of olivine crystals) is located primarily within the asthenosphere as a result of finite strain. There are two primary factors influencing the finite strain within the asthenosphere: (1) the motion of the Pacific plate relative to the deeper mantle (APM), and (2) density–buoyancy driven mantle flow. Both processes may have influenced finite strain history within the asthenosphere layers. Using the 'HC' semi-analytical, propagator matrix approach for calculating mantle circulation (Hager & O'Connell 1981; Milner *et al*. 2009), we generate global mantle flow models to address the contributions from density–buoyancy driven mantle flow and APM. We investigate the effects of APM and density–buoyancy driven mantle flow separately, and then investigate their combined effects. The mantle density variations are inferred using tomography models. Three fundamental inputs are required in HC: the mantle density perturbation, the depth-dependent effective viscosity and the scaling factor for density to seismic velocity ($dln\rho/dlnv_s$). In order to generate a distribution of mantle density perturbations, we tested four tomography models. These models were chosen because they show favourable global predictions for plate motions, stresses within the plates and strain rates within the plate boundary zones (Wang *et al*. 2015).

Table 3. Stacked shear wave splitting parameters obtained at OBS locations. The direction φ of shear wave polarization is measured clockwise from north, with one-sigma error $\pm\varphi$. δt indicates splitting delay times, with one-sigma error $\pm\delta t$. Note that some stations only had data from one event. See Fig. 1 for station locations.

Station	Latitude (°N)	Longitude (°E)	φ (°)	δt (s)	$\pm\varphi$ (°)	$\pm\delta t$ (s)	Earthquakes used
3	33.0129	−118.9574	85	1.7	9.5	0.35	1, 6, 7
8	32.7422	−120.7265	76	0.8	23	0.25	1, 7
10	33.3109	−122.1951	66	1.1	3	0.10	1
11	32.6645	−122.3016	71	1.2	9.5	0.15	1, 6, 7
13	32.6550	−123.8286	74	1.2	10.5	0.20	1, 3, 6, 7
15	33.3157	−124.6472	90	1.7	3.5	0.15	1, 5, 6, 7
18	33.2999	−123.8685	68	1.1	7	0.20	2
19	33.3021	−123.0373	72	1.0	17	0.25	1, 2, 3, 5, 6, 7
22	34.0978	−121.6617	62	1.1	8	0.30	4
28	33.5433	−119.4645	95	1.8	3.5	0.20	1, 5, 7
32	33.2085	−118.4802	78	0.8	21	0.20	6

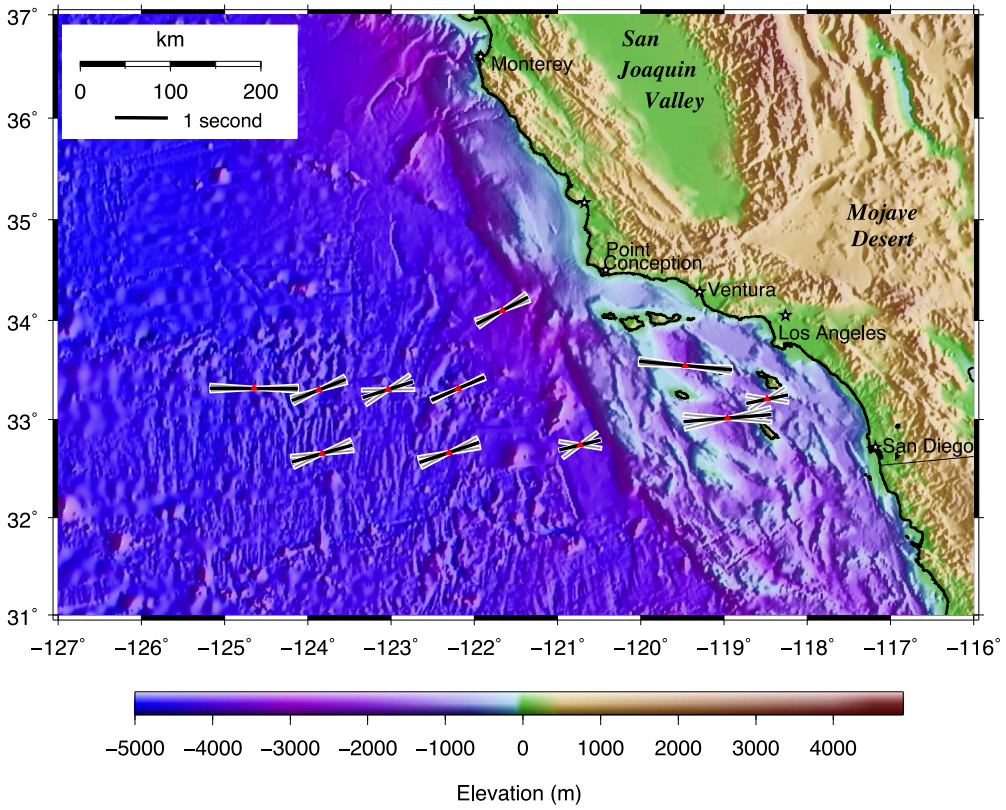

Figure 4. SKS splitting results for teleseismic earthquake signals recorded by the offshore southern California ALBACORE OBSs. Parameter values are shown in Table 3. Black line segments show computed value for splitting direction, and length of line is proportional to delay time. Grey line segments show one-sigma error range for splitting directions.

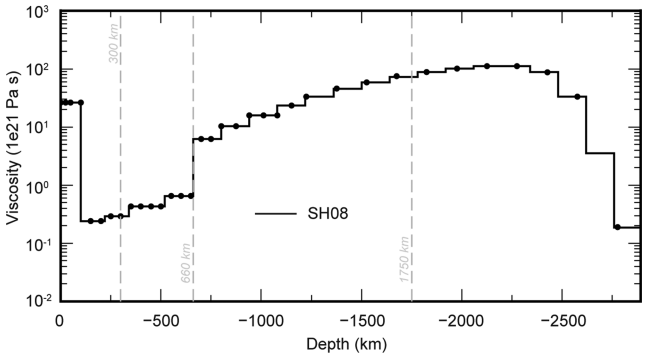

Figure 5. Viscosity model from Steinberger & Holme (2008) (SH08) used in the dynamic flow calculations.

Mantle convection is strongly influenced by the radial variation of viscosity (Bunge *et al*. 1996; Mitrovica & Forte 1997, 2004). Wang *et al*. (2015) argued that the viscosity model of Steinberger & Holme (2008; Fig. 5), when used to compute the influence of mantle convection calculations on lithospheric stresses, provides a better match to surface observables than other recently published radial viscosity models. This viscosity model (SH08) was also used by Davies *et al*. (2014). Viscosity model SH08 has a moderately strong lithosphere (~2×10^{22} Pa s), a moderately weak asthenosphere (~2×10^{20} Pa s) and a significant increase (from ~6×10^{20} to ~6×10^{21} Pa s) at 660 km below sea level (Fig. 5). The maximum viscosity (~1×10^{23} Pa s) is at about 2200 km, and there is a viscosity drop near the base of the mantle. Wang *et al*. (2015) also showed that the magnitude of the deviatoric stresses contributed by mantle convection is appropriate for most of the tested tomography models using a velocity-density scaling of 0.25 for *S*-wave models (Ghosh *et al*. 2013a) and 0.40 for *P*-wave models (Becker 2012). We thus adopt these scaling relations in this study.

A number of models have been proposed to explain the link between finite strain and expected LPO of olivine crystals within the upper mantle (Ribe 1992; Kaminski & Ribe 2001, 2002; Becker *et al*. 2003, 2006; Kaminski *et al*. 2004; Conrad *et al*. 2007; Long & Becker 2010). Becker *et al*. (2006) suggested that instantaneous mantle circulation from HC could be assumed to be in steady state for the time of LPO formation. This implies that models are most appropriate for the last ~10 Ma (Becker *et al*. 2008). Following Becker *et al*. (2003) and Becker *et al*. (2006), we calculate LPO using the D-REX implementation (Kaminski *et al*. 2004) by tracking velocity gradients along streamlines. D-REX takes into account enstatite in the aggregates and grain-boundary sliding of small grains based on kinematic theory (Kaminski & Ribe 2001, 2002). All parameters (dynamic recrystallization, and a 70 per cent olivine/30 per cent enstatite mineral assemblage, etc.) for the kinematic method are adopted from Kaminski *et al*. (2004).

We compute both the anisotropy effects and horizontal mantle flow velocity from APM (Figs 6 and 7) and density–buoyancy driven flow with no-slip boundary conditions (Figs 8 and 9) separately, and then investigate their combined influences (Fig. 10). Becker *et al*. (2006, 2008, 2012) argued that formation of LPO anisotropy for olivine in the dislocation-creep region can be quantitatively linked to anisotropy in the asthenosphere zone above ~300 km. Based on these studies, we focus anisotropy formation within the depth zones of 150–250 km within the asthenosphere. The effects of buoyancy driven mantle flow are computed using no-slip boundary conditions (Figs 8 and 9). The effects of APM alone (Figs 6 and 7) are

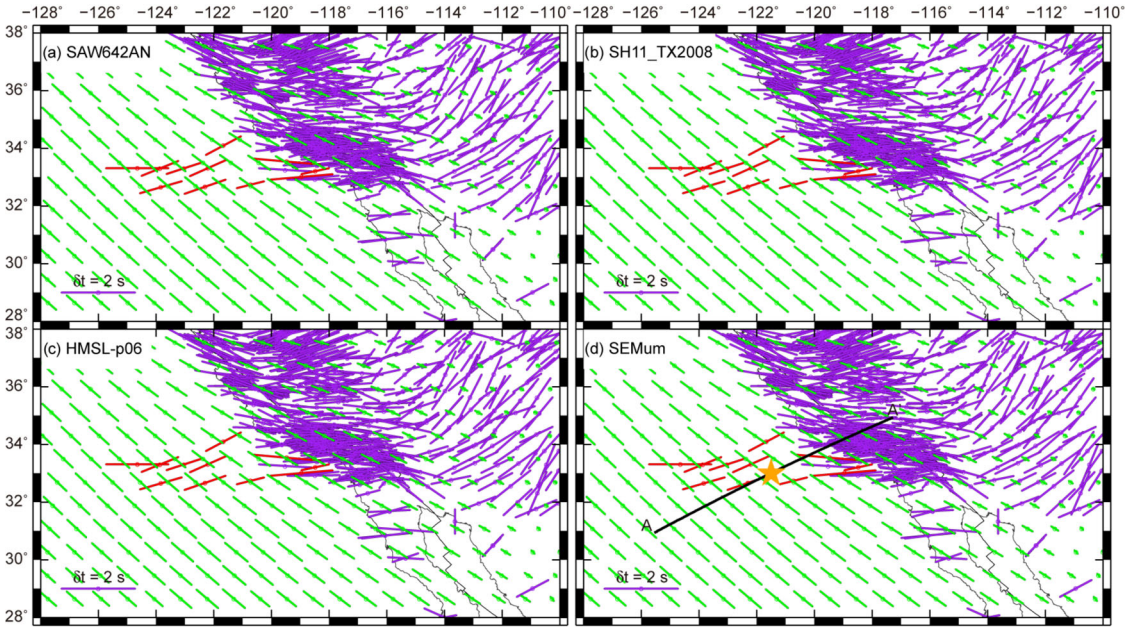

Figure 6. Depth-averaged (150–250 km) anisotropy fast polarization directions (green) from the effects of finite strain associated with absolute plate motion (APM; HS3-NUVEL-1A, Gripp & Gordon 2002) plotted on top of SKS splitting directions (red vectors: this study; purple vectors: compiled by Becker *et al.* 2012). Four models are shown, calculated by subtracting the effects of density–buoyancy driven mantle flow (with no-slip boundary conditions) from a total model that has velocity boundary conditions of APM together with density–buoyancy driven mantle flow effects. APM effects computed from models that had density–buoyancy flow obtained from (a) model SAW642AN (Panning & Romanowicz 2006), (b) model SH11_TX2008 (Simmons *et al.* 2009; Schmandt & Humphreys 2010, 2011; Becker 2012), (c) model HMSL-p06 (Houser *et al.* 2008) and (d) model SEMum (Lekić & Romanowicz 2011). Profile A–A′ shows location of cross-sections in Fig. 11.

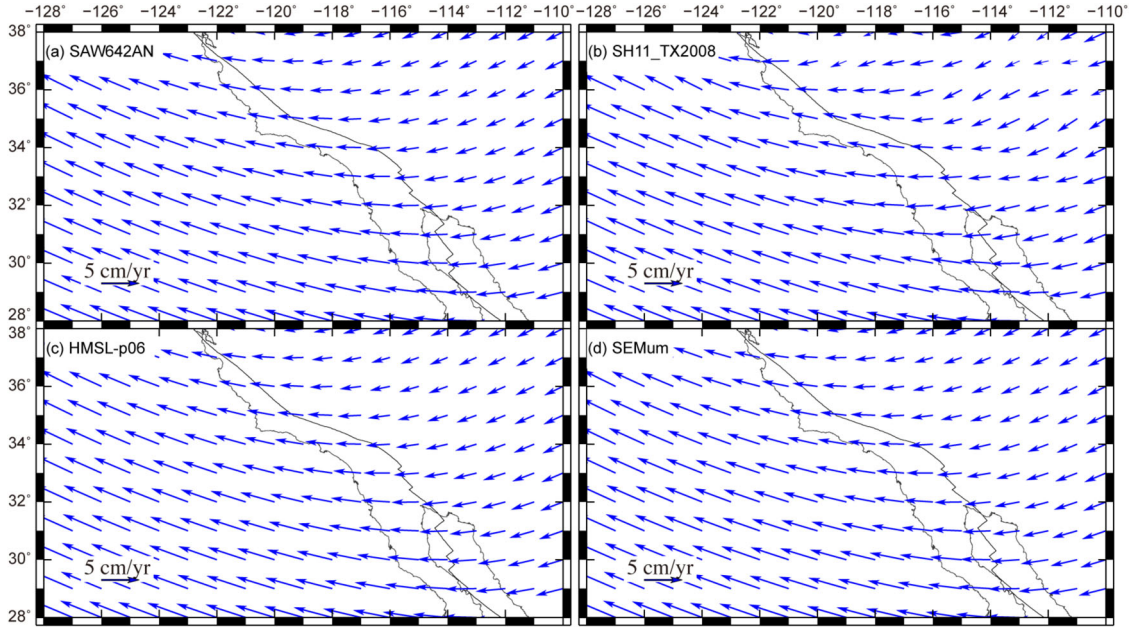

Figure 7. Depth-averaged horizontal component of mantle flow velocity (150–250 km) associated with APM effects only, computed as described in Fig. 6, for (a) model SAW642AN (Panning & Romanowicz 2006), (b) model SH11_TX2008 (Simmons *et al.* 2009; Schmandt & Humphreys 2010, 2011; Becker 2012), (c) model HMSL-p06 (Houser *et al.* 2008) and (d) model SEMum (Lekić & Romanowicz 2011).

computed by first calculating the full mantle flow field (including effects of buoyancy driven mantle flow) with imposed surface boundary conditions of APM [HS3-NUVEL-1A (Gripp & Gordon 2002)], and then second by subtracting out the effects of buoyancy-related flow alone, computed using no-slip boundary conditions. This procedure yields identical results for plate motion effects, regardless of which tomography model is used in the original full calculation of mantle flow (Figs 6 and 7). We compute anisotropy at depths of 150, 200 and 250 km, and then compute depth-averaged anisotropy values (Figs 6, 8 and 10) that can be compared with the observed SKS splitting fast-polarization directions. Below we discuss the effects of APM alone, buoyancy driven mantle flow alone, and full mantle convection from both APM and buoyancy driven flow.

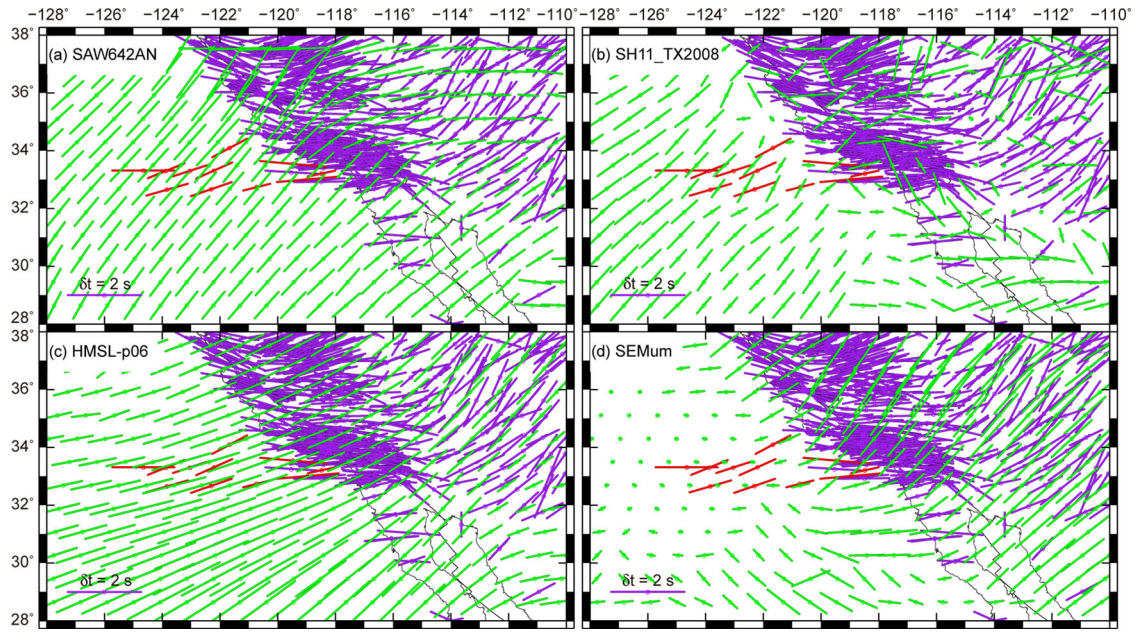

Figure 8. Depth-averaged (150–250 km) anisotropy fast polarization directions (green) associated with density–buoyancy driven mantle flow shown in Fig. 9, computed with no-slip boundary conditions and obtained from tomography models (a) SAW642AN (Panning & Romanowicz 2006), (b) SH11_TX2008 (Simmons *et al*. 2009; Schmandt & Humphreys 2010, 2011; Becker 2012), (c) HMSL-p06 (Houser *et al*. 2008) and (d) SEMum (Lekić & Romanowicz 2011). Predicted anisotropy fast polarization directions are plotted together with SKS splitting directions (red vectors: this study; purple vectors: compiled by Becker *et al*. 2012).

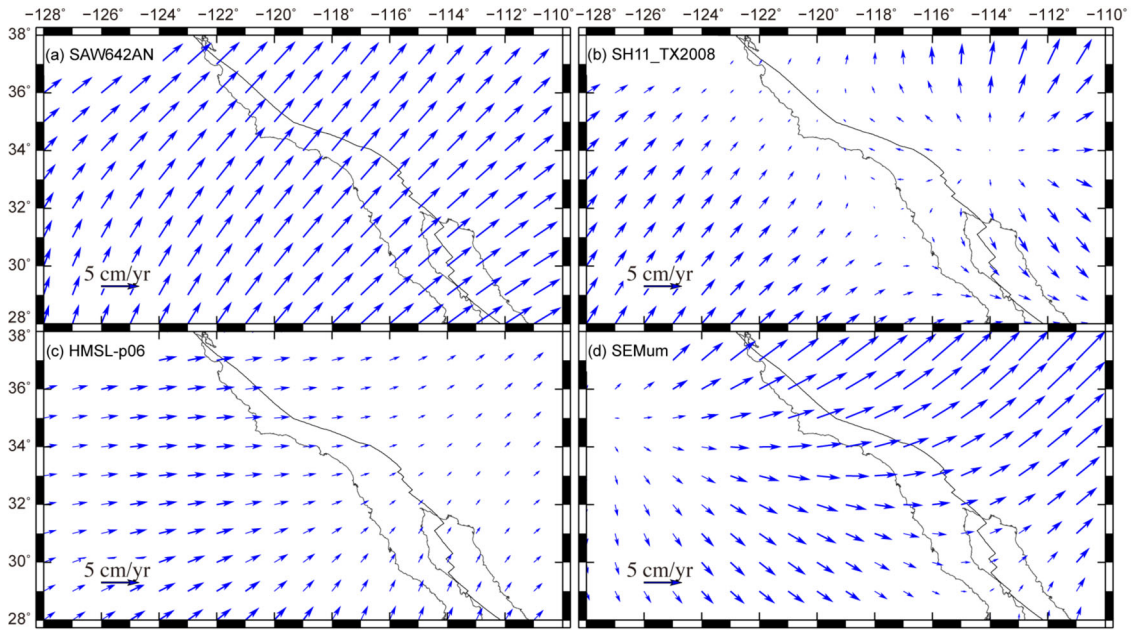

Figure 9. Depth-averaged horizontal component of mantle flow velocity (150–250 km) associated with density–buoyancy driven flow with no-slip boundary conditions obtained from tomography models (a) SAW642AN (Panning & Romanowicz 2006), (b) SH11_TX2008 (Simmons *et al*. 2009; Schmandt & Humphreys 2010, 2011; Becker 2012), (c) HMSL-p06 (Houser *et al*. 2008) and (d) SEMum (Lekić & Romanowicz 2011).

THE INFLUENCE OF PLATE MOTION ALONE

Fast polarization directions and splitting delay times predicted from APM-developed anisotropy within the finite strain field of the asthenosphere between depths of 150–250 km differ from observed directions (Fig. 6). These results are similar to calculations of APM effects (no-net-rotation frame) of Becker *et al*. (2003). Predicted directions are not consistent with the new observations of SKS fast orientations in the Pacific plate presented here (Fig. 4), nor are they consistent with observations of SKS splitting within the plate boundary zone interior. It is clear that upper-mantle anisotropy throughout the Pacific-western U.S. plate boundary zone has a significant influence from factors other than APM alone (e.g. Becker *et al*. 2003, 2006).

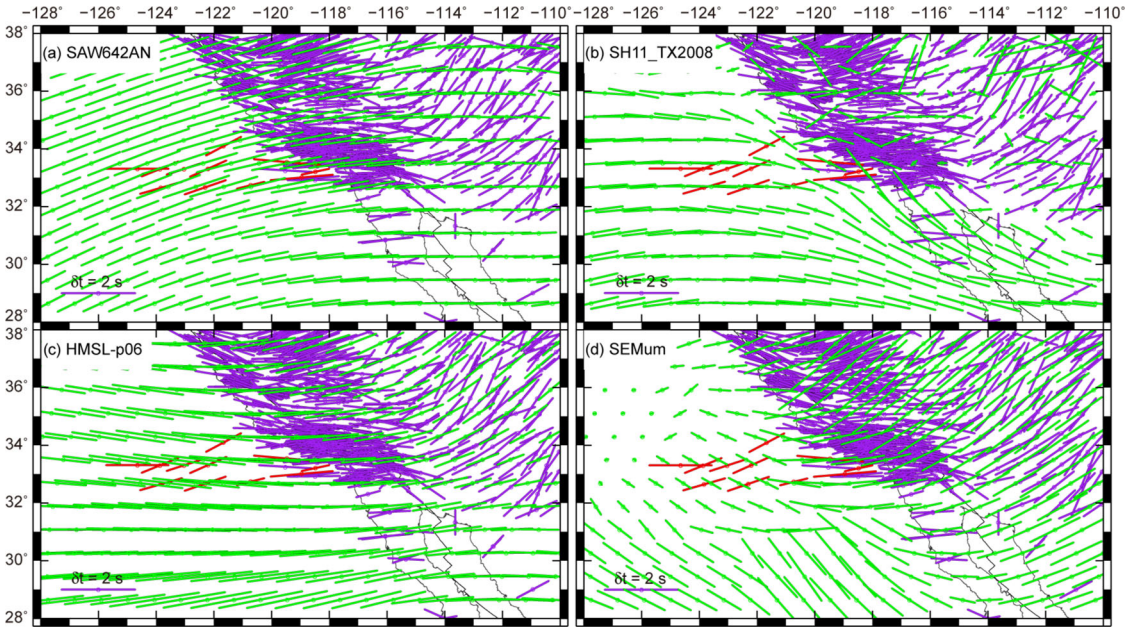

Figure 10. Depth-averaged (150–250 km) anisotropy fast polarization directions (green) associated with combined effects of APM (HS3-NUVEL-1A, Gripp & Gordon 2002) and density–buoyancy driven flow, where mantle flow calculations were obtained from (a) model SAW642AN (Panning & Romanowicz 2006), (b) model SH11_TX2008 (Simmons *et al*. 2009; Schmandt & Humphreys 2010, 2011; Becker 2012), (c) model HMSL-p06 (Houser *et al*. 2008) and (d) model SEMum (Lekić & Romanowicz 2011). Predicted anisotropy fast polarization directions together with SKS splitting directions (red vectors: this study; purple vectors: compiled by Becker *et al*. 2012).

THE INFLUENCE OF BUOYANCY-DRIVEN MANTLE FLOW ALONE

After the method described by Ghosh *et al*. (2013b), Wang *et al*. (2015) used published global tomography models as constraints for global, forward-model, mantle convection calculations in which they evaluated the contribution these models make toward fitting stress orientations, strain rates and the geoid. We chose to evaluate four tomography models that Wang *et al*. (2015) found to provide reasonable matches to observations globally [SAW642AN (Panning & Romanowicz 2006), SH11_TX2008 (Schmandt & Humphreys 2010, 2011; Becker 2012), HMSL-p06 (Houser *et al*. 2008) and SEMum (Lekić & Romanowicz 2011)]. For simplicity of discussion, the mantle flow directions that we refer to that are associated with influences of mantle density–buoyancies are in isolation of the effects of APM (computed with no-slip boundary conditions). Actual full mantle flow directions, and the LPO fabric they produce (Figs 10 and 11), include the effects of both plate motions (Figs 6 and 7) and density–buoyancy driven mantle flow (Figs 8 and 9). With no-slip boundary conditions, all models predict an overall E–NE upper-mantle flow towards North America (blue vectors in Fig. 9). This horizontal mantle flow pattern beneath this portion of the Pacific plate (Fig. 9) is strongly influenced by a very long-wavelength, large-scale downwelling beneath central North America, which can be linked with the foundering of higher-density slab material, both above and below transition zone depths (Lithgow-Bertelloni & Richards 1998; Steinberger 2000; Becker & O'Connell 2001; Silver & Holt 2002). There is variability in the flow directions and in the eastward extent of depth-averaged horizontal flow (150–250 km) for the various models. Model SAW642AN shows a more NE-directed flow than any other model and this flow persists both beneath the Pacific plate and beneath much of the western North America plate boundary zone (Fig. 9a). Depth-averaged anisotropy directions (Fig. 8a) from this model are likewise NE-oriented. Directions of mantle flow and anisotropy from model HMSL-p06 (Figs 9c and 8c) are oriented E–NE. Mantle flow motions from SH11_TX2008 and SEMum (Figs 9b and d) are more variable in flow direction, with the former showing considerable variation in directions of anisotropy (Fig. 8b) owing to the fact that it is a model derived from higher-resolution tomography.

COMBINED EFFECTS OF PLATE MOTION AND DENSITY–BUOYANCY DRIVEN MANTLE FLOW

The combined effects of plate motion and density–buoyancy driven mantle flow from the four models investigated show agreement with observations in some regions and considerable disagreement in others (Fig. 10). Model SAW642AN (Fig. 10a) provides the best agreement with SKS observations within the Pacific plate from this study. Model SAW642AN also provides a good fit within southern California. However, this model does a poor job of predicting SKS splitting orientations within central California and within the western Basin and Range. Whereas model HMSL-p06 (Fig. 10c) does not match the Pacific plate observations as closely as SAW642AN, it provides a better fit within northern California, southern California, and the western Basin and Range. The remaining two models (SH11_TX2008 and SEMum, Figs 10b and d) do not in general provide a good fit to SKS splitting directions. Although no single model matches observations everywhere, the properties in HMSL-p06 (Fig. 10c) provide the closest overall match with observations. Additional Figs S8–S15 in Supporting Information show anisotropy calculations for the four separate models investigated at depths of 150, 200, 250, 250 and 300 km. These are for both the no-slip boundary condition models and for the total models (APM + density–buoyancy driven flow).

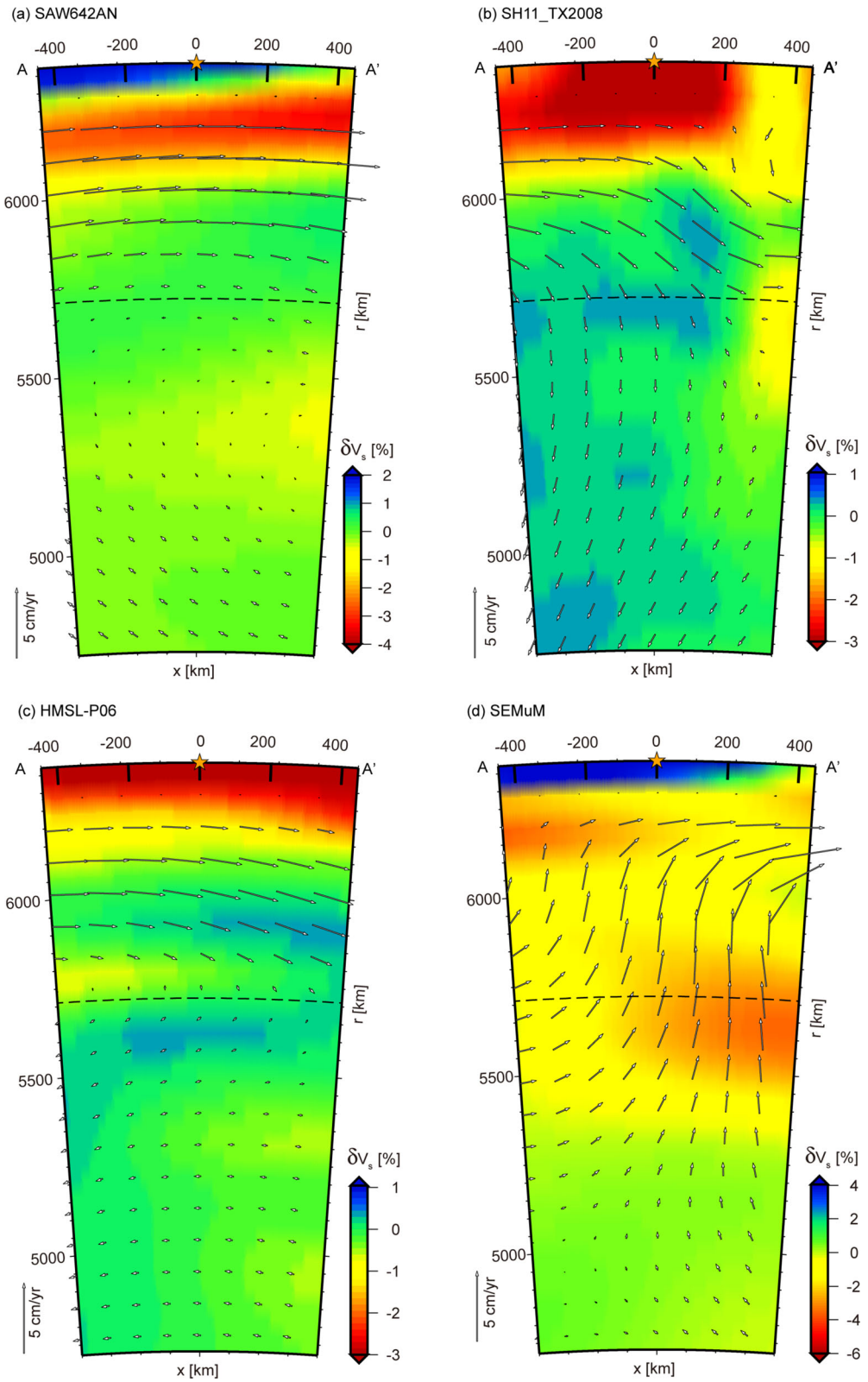

Figure 11. Mantle flow profiles for no-slip boundary conditions along A–A′ (see Fig. 6d) obtained from (a) model SAW642AN (Panning & Romanowicz 2006), (b) model SH11_TX2008 (Simmons *et al.* 2009; Schmandt & Humphreys 2010, 2011; Becker 2012), (c) model HMSL-p06 (Houser *et al.* 2008) and (d) model SEMum (Lekić & Romanowicz 2011).

IMPLICATIONS FOR MANTLE FLOW, AND THE ROLE OF PRESENT AND PAST SUBDUCTION

Comparing depth-averaged mantle flow fields (Fig. 9) associated with density–buoyancy driven mantle flow, the NE-directed flow, such as in model SAW642AN beneath the Pacific plate where the SKS measurements were made, provides the best match to the SKS orientations when combined with APM effects (Fig. 10a). However, NW-oriented SKS fast directions in central and northern California apparently require a diminished role of density–buoyancy driven mantle flow beneath these regions, as SKS splitting directions there agree closely with the predicted influence of APM alone (Fig. 6). Within southern California, SKS fast splitting directions require density–buoyancy driven mantle flow directions that are directed more easterly, such as for models HMSL-p06 and SEMum (Figs 9c and d). However, within the western Basin and Range, SKS fast splitting directions are most compatible with an influence in density–buoyancy driven mantle flow that is directed NE. The role of vertical flow adds a complication that is not represented by Fig. 9, which only shows horizontal components of flow. Predicted anisotropy in this study, however, also includes the influence of vertical components of mantle flow (Fig. 11).

Although the mantle flow models investigated show some variation in quality of fit to regional SKS patterns, they all yield some component of NE-directed flow (no-slip boundary conditions) associated with density–buoyancy mantle flow effects alone. This flow field, in combination with hotspot Pacific plate motion [HS3-NUVEL-1A (Gripp & Gordon 2002)], provides anisotropy directions that show first-order agreement with regional patterns of SKS splitting directions (Fig. 10). The NE-directed flow predicted by models that incorporate the effects of density–buoyancy driven mantle flow (no-slip boundary conditions, Fig. 11) are not in general consistent with the toroidal flow model of Zandt & Humphreys (2008), which would predict an E–SE mantle flow direction along the westernmost edge of North America, that is, southernmost edge of the Juan de Fuca slab. It is in this region of north-central California that apparently SKS splitting observations are most compatible with a minimum contribution from density–buoyancy driven mantle flow. Elsewhere, the addition of density–driven mantle flow is critical for explaining the SKS observations. Models that have smoother, longer-wavelength flow patterns associated with density–buoyancy driven mantle flow tend to provide a better match with SKS splitting directions, though directional changes in the mantle flow field are clearly required between offshore and onshore California, and between southern California and the western Basin and Range. Mantle flow impacting the western U.S. region beneath the Pacific plate thus appears to be long-wavelength (Figs 7 and 9), likely influenced by large-scale density variations associated with the long history of subduction beneath North America.

Within the interior western U.S. region, the more complex pattern of fast shear wave polarization directions (Silver 1996; Wüstefeld *et al*. 2009; Becker *et al*. 2012; Refayee *et al*. 2014) requires, at least for the western Basin and Range, density–buoyancy driven flow directions that are NE-directed. Within onshore southern California, best-fit directions of mantle flow associated with density–buoyancies are E–NE-directed. These directions are compatible with directions proposed by Silver & Holt (2002). Such a pattern in onshore southern California of E–NE directed flow and in western Basin and Range of NE-directed flow is also consistent with the toroidal flow model of Zandt & Humphreys (2008). Surprisingly, the higher-resolution model of SH11-TX2008 does not provide an improved fit to western Basin and Range SKS fast splitting directions (Fig. 10b). A full analysis of the entire western US region, and its link with mantle flow, is beyond the scope of this study.

CONCLUSIONS

SKS splitting measured on OBS stations off the coast of southern California exhibits WSW–ENE fast directions and splitting times of up to 2 s. The measurements extend the EW land-based observations on the North America plate hundreds of km west onto the Pacific plate. This is opposite the expectation that fast directions on the Pacific plate would rotate from EW to NW–SE to align with Pacific plate APM, and requires a different causative explanation involving deeper mantle flow. Various global mantle flow models were tested based on body forces from density contrasts inferred from tomography. These models show that the sub-asthenospheric mantle flow is strongly impacted by density–buoyancy driven mantle flow effects. These influences combine with APM to provide a total field of finite strain patterns that is complex. SKS observations require that this mantle flow field is laterally heterogeneous with spatially variable directions. SKS splitting measurements in this study for areas beneath the Pacific plate require a significant lateral variation in density–buoyancy driven mantle flow from NE-directed beneath the Pacific, transitioning to E–NE beneath southern California, and then back to NE-directed motions again beneath the western Basin and Range. In central and northern California there is apparently a diminishing impact from density–buoyancy driven flow, as SKS splitting directions there agree with the effects of APM alone (Fig. 6). The main source of the long-wavelength component of the density–buoyancy driven flow is from the sinking of previously subducted material now beneath interior North America (Sigloch & Mihalynuk 2013). No single model is able to predict all regional variations from onshore to offshore, suggesting that the LPO-producing mechanism within the asthenosphere depends on both APM and density–buoyancy driven flow; this dependence varies significantly over lateral length scales equivalent to the asthenosphere thickness. Refined models of density–driven mantle flow are needed, and the new coverage added by the SKS observations in this study provides important new constraints for mantle flow models. Our results suggest that motions of sub-asthenospheric mantle that are associated with density–buoyancy driven mantle flow can be as large as or larger than APM, which if taken into account may reconcile the global measurements.

ACKNOWLEDGEMENTS

We acknowledge Brian Clements for providing the horizontal-component orientation measurements used in this study, and we thank Thorsten Becker for his help and sharing of codes. The OBS waveform data from the ALBACORE array are available from the IRIS Data Management Center. The IRIS Data Management System is funded through the National Science Foundation, specifically the GEO Directorate through the Instrumentation and Facilities Program under Cooperative Agreement EAR-1063471. The OBS deployment was made possible with instruments and logistical support of the IRIS Ocean Bottom Seismic Instrumentation Pool (OBSIP); in particular, thanks go to Jeff Babcock, Ernie Aaron, Phil Thai and Mark Gibaud at Scripps Institution of Oceanography. The ALBACORE OBS deployment and recovery cruises were made possible with the equipment and logistical support of the University-National Oceanographic Laboratory System (UNOLS) vessel fleet and staff

support at Scripps with particular thanks to Jon Meyer, Brian Rowe and Meghan Donohue. MDK and DSW thank Captain Curl and the crew of R/V Melville for assistance during the 2010 OBS deployment cruise, and Captain Vullo and the crew of R/V New Horizon during the 2011 OBS recovery cruise. This work was supported by the National Science Foundation (grant # OCE-0825254).

REFERENCES

Amante, C. & Eakins, B.W., 2009. ETOPO1 1 arc-minute global relief model: procedures, data sources and analysis, *NOAA Technical Memorandum NESDIS NGDC-24,* 19 pp.

Anderson, O.L. & Isaak, D.G., 1995. Elastic constants of mantle minerals at high temperature, in *Mineral Physics and Crystallography: A Handbook of Physical Constants*, pp. 64–97, ed. Ahrens, T.J., American Geophysical Union.

Atwater, T., 1970. Implications of plate tectonics for the Cenozoic tectonic evolution of Western North America, *Geol. Soc. Am. Bull.,* **81,** 3513–3536.

Atwater, T., 1989. Plate tectonic history of the northeast Pacific and western North America, in *The Geology of North America Vol. N., The Eastern Pacific Ocean and Hawaii,* Geological Society of America.

Barruol, G., Suetsugu, D., Shiobara, H., Sugioka, H., Tanaka, S., Bokelmann, G.H.R., Fontaine, F.R. & Reymond, D., 2009. Mapping upper mantle flow beneath French Polynesia from broadband ocean bottom seismic observations. *Geophys. Res. Lett.,* **36**(14), doi:10.1029/2009GL038139.

Becker, T.W., 2012. On recent seismic tomography for the western United States, *Geochem. Geophys. Geosyst.,* **13,** Q01W10, doi:10.1029/2011GC003977.

Becker, T.W. & O'Connell, R.J., 2001. Predicting plate velocities with mantle circulation models, *Geochem. Geophys. Geosyst.,* **2**(12), 1060, doi:10.1029/2001GC000171.

Becker, T.W., Kellogg, J.B., Ekström, G. & O'Connell, R.J., 2003. Comparison of azimuthal seismic anisotropy from surface waves and finite-strain from global mantle-circulation models, *Geophys. J. Int.,* **155,** 696–714.

Becker, T.W., Chevrot, S., Schulte-Pelkum, V. & Blackman, D.K., 2006. Statistical properties of seismic anisotropy predicted by upper mantle geodynamic models, *J. geophys. Res.,* **111**(B8), doi:10.1029/2005JB004095.

Becker, T.W., Kustowski, B. & Ekstrom, G., 2008. Radial seismic anisotropy as a constraint for upper mantle rheology, *Earth planet. Sci. Lett.,* **267**(1–2), 213–227.

Becker, T.W., Lebedev, S. & Long, M.D., 2012. On the relationship between azimuthal anisotropy from shear wave splitting and surface wave tomography, *J. geophys. Res.,* **117**(B1), doi:10.1029/2011JB008705.

Beghein, C., Yuan, K., Schmerr, N. & Xing, Z., 2014. Changes in seismic anisotropy shed light on the nature of the gutenberg discontinuity, *Science,* **343**(6176), 1237–1240.

Bowden, D.C., Kohler, M.D., Tsai, V.C. & Weeraratne, D.S., 2016. Offshore Southern California lithospheric velocity structure from noise cross-correlation functions, *J. geophys. Res.,* **121,** doi:10.1002/2016JB012919.

Bunge, H.-P., Richards, M.A. & Baumgardner, J.R., 1996. Effect of depth-dependent viscosity on the planform of mantle convection, *Nature,* **379**(6564), 436–438.

Conrad, C.P., Behn, M.D. & Silver, P.G., 2007. Global mantle flow and the development of seismic anisotropy: differences between the oceanic and continental upper mantle, *J. geophys. Res.,* **112,** B07317, doi:10.1029/2006JB004608.

Crouch, J.K. & Suppe, J., 1993. Late Cenozoic tectonic evolution of the Los Angeles Basin and inner California borderland: a model for core complex-like crustal extension, *Bull. geol. Soc. Am.,* **105,** 1415–1434.

Crowell, J.C., 1968. Movement histories of faults in the Transverse ranges and speculations on the tectonic history of California, in *Proceedings of the Conference on Geologic Problems of the San Andreas Fault System*, Vol. **11**, pp. 323–341, eds Dickinson, W.R. & Grantz, A., Stanford Univ. Publ. Geol. Sci.

Davies, C.J., Stegman, D.R. & Dumberry, M., 2014. The strength of gravitational core-mantle coupling, *Geophys. Res. Lett.,* **41**(11), 3786–3792.

Dokka, R.K., 1989. The Mojave extensional belt of Southern California, *Tectonics,* **8,** 363–390.

Engebretson, D.C., Cox, A. & Gordon, R.G., 1985. Relative motions between oceanic and continental plates in the Pacific basin, *Geol. Soc. Am. Spec. Pap.,* **206,** 1–60.

Feigl, K.L. *et al.*, 1993. Space geodetic measurement of crustal deformation in central and Southern California, 1984–1992, *J. geophys. Res.,* **98,** 21 677–21 712.

Ghosh, A., Becker, T.W. & Humphreys, E.D., 2013a. Dynamics of the North American continent, *Geophys. J. Int.,* **194**(2), 651–669.

Ghosh, A., Holt, W.E. & Wen, L.M., 2013b. Predicting the lithospheric stress field and plate motions by joint modeling of lithosphere and mantle dynamics, *J. geophys. Res.,* **118**(1), 346–368.

Gripp, A.E. & Gordon, R.G., 2002. Young tracks of hotspots and current plate velocities, *Geophys. J. Int.,* **150**(2), 321–361.

Hager, B.H. & O'Connell, R.J., 1981. A simple global model of plate dynamics and mantle convection, *J. geophys. Res.,* **86**(B6), 4843–4867.

Harmon, N., Forsyth, D.W., Fischer, K.M. & Webb, S.C., 2004. Variations in shear-wave splitting in young pacific seafloor, *Geophys. Res. Lett.,* **31**(15), doi:10.1029/2004GL020495.

Houser, C., Masters, G., Shearer, P. & Laske, G., 2008. Shear and compressional velocity models of the mantle from cluster analysis of long-period waveforms, *Geophys. J. Int.,* **174**(1), 195–212.

Kaminski, É. & Ribe, N.M., 2001. A kinematic model for recrystallization and texture development in olivine polycrystals, *Earth planet. Sci. Lett.,* **189,** 253–267.

Kaminski, E. & Ribe, N.M., 2002. Timescales for the evolution of seismic anisotropy in mantle flow, *Geochem. Geophys. Geosyst.,* **3,** doi:10.1029/2001GC000222.

Kaminski, É., Ribe, N.M. & Browaeys, J.T., 2004. D-Rex, a program for calculation of seismic anisotropy due to crystal lattice preferred orientation in the convective upper mantle. *Geophys. J. Int.,* **158,** 744–752.

Kohler *et al.*, 2010. ALBACORE OBS deployment cruise report, 27 pp., R/V Melville Cruise MV1010, kohler.caltech.edu/Offshore/ALBACORE_2010_Cruise_Report.pdf (last accessed August 14–27).

Kohler *et al.*, 2011. ALBACORE OBS recovery cruise report, 35 pp., R/V New Horizon Cruise NH1111, kohler.caltech.edu/Offshore/ALBACORE_2011_Cruise_Report.pdf (last accessed September 7–16).

Kosarian, M., Davis, P.M., Tanimoto, T. & Clayton, R.W., 2011. The relationship between upper mantle anisotropic structures beneath California, transpression, and absolute plate motions, *J. geophys. Res.,* **116**(B8), doi:10.1029/2010JB007742.

Lekić, V. & Romanowicz, B., 2011. Inferring upper-mantle structure by full waveform tomography with the spectral element method, *Geophys. J. Int.,* **185**(2), 799–831.

Lithgow-Bertelloni, C. & Richards, M.A., 1998. The dynamics of Cenozoic and Mesozoic plate motions, *Rev. Geophys,* **36**(1), 27–78.

Liu, H., Davis, P.M. & Gao, S., 1995. SKS splitting beneath Southern California, *Geophys Res. Lett.,* **22,** 767–770.

Liu, Z. & Bird, P., 2002. North America plate is driven westward b lower mantle flow, *Geophys. Res. Lett.,* **29,** doi:10.1029/2002GL016002.

Long, M.D. & Becker, T.W., 2010. Mantle dynamics and seismic anisotropy, *Earth planet. Sci. Lett.,* **297,** Frontiers, 341–354.

Luyendyk, B.P., 1991. A model for Neogene crustal rotations, transtension, and transpression in southern California, *Bull. geol. Soc. Am.,* **103,** 1528–1536.

Milner, K., Becker, T.W., Boschi, L., Sain, J., Schorlemmer, D. & Waterhouse, H., 2009. New Software Framework to Share Research Tools, *EOS, Trans. Am. geophys. Un.,* **90**(12), 104–104.

Mitrovica, J.X. & Forte, A.M., 1997. Radial profile of mantle viscosity: Results from the joint inversion of convection and postglacial rebound observables, *J. geophys. Res.,* **102**(B2), 2751–2769.

Mitrovica, J.X. & Forte, A.M., 2004. A new inference of mantle viscosity based upon joint inversion of convection and glacial isostatic adjustment data, *Earth planet. Sci. Lett.,* **225**(1–2), 177–189.

Montagner, J.-P., Griot-Pommera, D.-A. & Lave, J., 2000. How to relate body wave and surface wave anisotropy?, *J. geophys. Res.,* **105**(B8), 19 015–19 027.
Monteiller, V. & Chevrot, S., 2011. High-resolution imaging of the deep anisotropic structure of the San Andreas Fault system beneath southern California, *Geophys. J. Int.,* **186,** 418–446.
Özalaybey, S. & Savage, M.K., 1995. Shear-wave splitting beneath western United States in relation to plate tectonics, *J. geophys. Res.,* **100,** 18 135–18 149.
Panning, M. & Romanowicz, B., 2006. A three-dimensional radially anisotropic model of shear velocity in the whole mantle, *Geophys. J. Int.,* **167**(1), 361–379.
Polet, J. & Kanamori, H., 2002. Anisotropy beneath California: shear wave splitting measurements using a dense broadband array, *Geophys. J. Int.,* **149,** 313–327.
Reeves, Z., Lekic, V., Schmerr, N., Kohler, M.D. & Weeraratne, D., 2015. Lithospheric structure across the continental borderland from receiver functions, *Geochem. Geophys. Geosyst.,* **15,** 246–266.
Refayee, H.A., Yang, B.B., Liu, K.H. & Gao, S.S., 2014. Mantle flow and lithosphere–asthenosphere coupling beneath the southwestern edge of the North American craton: constraints from shear-wave splitting measurements, *Earth planet. Sci. Lett.,* **402,** 209–220.
Ribe, N.M., 1992. On the relation between seismic anisotropy and finite strain, *J. geophys. Res.,* **97,** 8737–8747.
Ribe, N.M. & Yu, Y., 1991. A theory for plastic deformation and textural evolution of olivine polycrystals, *J. geophys. Res.,* **96,** 8325–8335.
Savage, M.K., Silver, P.G. & Meyer, R.P., 1990. Observations of teleseismic shear-wave splitting in the Basin and Range from portable and permanent stations, *Geophys. Res. Lett.,* **17,** 21–24.
Schmandt, B. & Humphreys, E., 2010. Complex subduction and small-scale convection revealed by body-wave tomography of the western United States upper mantle, *Earth planet. Sci. Lett.,* **297**(3–4), 435–445.
Schmandt, B. & Humphreys, E., 2011. Seismically imaged relict slab from the 55 Ma Siletzia accretion to the northwest United States, *Geology,* **39**(2), 175–178.
Shen, Z., Jackson, D.D. & Ge, B.X., 1996. Crustal deformation across and beyond the Los Angeles basin from geodetic measurements, *J. geophys. Res.,* **101,** 27 957–27 980.
Sigloch, K. & Mihalynuk, M.G., 2013. Intra-oceanic subduction shaped the assembly of Cordilleran North America, *Nature,* **496**(7443), 50–56.
Silver, P.G., 1996. Seismic anisotropy beneath the continents: probing the depths of Geology, *Annu. Rev. Earth Planet. Sci.,* **24,** 385–432.
Silver, P.G. & Chan, W.W., 1991. Shear wave splitting and subcontinental mantle deformation, *J. geophys. Res.,* **96**(B10), 16 429–16 454.
Silver, P.G. & Holt, W.E., 2002. The mantle flow field beneath western North America, *Science,* **295**(5557), 1054–1057.
Silver, P.G. & Savage, M.K., 1994. The interpretation of shear-wave splitting parameters in the presence of two anisotropic layers. *Geophys. J. Int.,* **119,** 949–963.
Simmons, N.A., Forte, A.M. & Grand, S.P., 2009. Joint seismic, geodynamic and mineral physical constraints on three-dimensional mantle heterogeneity: implications for the relative importance of thermal versus compositional heterogeneity, *Geophys. J. Int.,* **177**(3), 1284–1304.
Stachnik, J.C., Sheehan, A.F., Zietlow, D.W., Yang, Z., Collins, J. & Ferris, A., 2012. Determination of New Zealand ocean bottom seismometer orientation via Rayleigh-wave polarization, *Seismol. Res. Lett.,* **83,** 704–713.
Steinberger, B., 2000. Slabs in the lower mantle - results of dynamic modelling compared with tomographic images and the geoid, *Phys. Earth planet. Inter.,* **118**(3–4), 241–257.
Steinberger, B. & Holme, R., 2008. Mantle flow models with core-mantle boundary constraints and chemical heterogeneities in the lowermost mantle, *J. geophys. Res.,* **113**(B5), B05403, doi:10.1029/2007JB005080.
Stock, J.M. & Hodges, K.V., 1989. Pre-Pliocene extension around the Gulf of California and the transfer of Baja California to the Pacific plate, *Tectonics,* **8,** 99–115.
Tennyson, M.E., 1989. Pre-transform early Miocene extension in western California, *Geology,* **17,** 792–796.
Vinnik, L.P., Farra, V. & Romanowicz, B., 1989. Aziumuthal anisotropy in the Earth from observations of SKS at Geoscope and NARS broadband stations, *Bull. seism. Soc. Am.,* **79,** 1542–1558.
Walls, C., Rockwell, T., Mueller, K., Bock, Y., Williams, S., Pfanner, J., Dolan, J. & Fang, P., 1998. Escape tectonics in the Los Angeles metropolitan region and implications for seismic risk, *Nature,* **394,** 356–360.
Walsh, E., Arnold, R. & Savage, M.K., 2013. Silver and Chan revisted, *J. geophys. Res.,* **118,** 550–5515.
Wang, X., Holt, W.E. & Ghosh, A., 2015. Joint modeling of lithosphere and mantle dynamics: Evaluation of constraints from global tomography models, *J. geophys. Res.,* **120**(12), 8633–8655.
Weeraratne, D.S., Forsyth, D.W., Yang, Y. & Webb, S.C., 2007. Rayleigh wave tomography beneath intraplate volcanic ridges in the South Pacific, *J. geophys. Res.,* **112,** B06303, doi:10.1029/2006JB004403.
West, J.D., Fouch, M.J., Roth, J.B. & Elkins-Tanton, L.T., 2009. Vertical mantle flow associated with a lithospheric drip beneath the great basin, *Nat. Geosci.,* **2,** 439–444.
Wolfe, C.J. & Silver, P.G., 1998. Seismic anisotropy of oceanic upper mantle: shear wave splitting methodologies and observations, *J. geophys. Res.,* **103**(B1), 749–771.
Wolfe, C.J. & Solomon, S.C., 1998. Shear-wave splitting and implications for mantle flow beneath the melt region of the East Pacific Rise, *Science,* **280**(5367), 1230–1232.
Wright, T.L., 1991. Structural geology and tectonic evolution of the Los Angeles basin, California, in *Active Margin Basins,* Vol. 52, pp. 35–134, ed. Biddle, K.T., AAPG Mem.
Wüstefeld, A., Bokelmann, G., Barruol, G. & Montagner, J.-P., 2009. Identifying global seismic anisotropy patterns by correlating shear-wave splitting and surface-wave data, *Phys. Earth planet. Inter.,* **176,** 198–212.
Yang, Y. & Forsyth, D.W., 2006. Rayleigh wave phase velocities, small-scale convection, and azimuthal anisotropy beneath southern California, *J. geophys. Res.,* **111,** B07306, doi:10.1029/2006JB004180.
Yuan, K. & Beghein, C., 2013. Seismic anisotropy changes across upper mantle phase transitions, *Earth planet. Sci. Lett.,* **374,** 132–144.
Zandt, G. & Humphreys, E., 2008. Toroidal mantle flow through the western U.S. slab window, *Geology,* **36**(4), 295–298.

SUPPORTING INFORMATION

Additional Supporting Information may be found in the online version of this paper:

Figure S1. Time window of processed data showing radial and transverse components.
Figure S2. Time window of processed data with the transverse component minimized.
Figure S3. Particle motion after minimizing transverse component energy.
Figure S4. Contour of transverse energy.
Figure S5. Stacked phi error measurements.
Figure S6. Stacked delay time error measurements.
Figure S7. Contour of transverse stacked energy.
Figure S8. Anisotropy fast polarization directions (green) associated with density buoyancy driven flow in Fig. 9, computed with no-slip boundary conditions and obtained from tomography model SAW642AN (Panning & Romanowicz 2006). Predicted anisotropy directions are plotted on top of SKS splitting directions (red vectors: this study; purple vectors: compiled by Becker *et al*. 2012) at (a) 150 km, (b) 200 km, (c) 250 km and (d) 300 km.
Figure S9. Same as Fig. S8, but for model SH11_TX2008 (Simmons *et al.* 2009; Schmandt & Humphreys 2010, 2011; Becker 2012).
Figure S10. Same as Fig. S8, but for model HMSL-p06 (Houser *et al*. 2008).
Figure S11. Same as Fig. S8, but for model SEMum (Lekić & Romanowicz 2011).

Figure S12. Anisotropy fast polarization directions (green) associated with effects of APM (HS3-NUVEL-1A, Gripp & Gordon 2002) and density buoyancy driven flow (Fig. 10) from model SAW642AN (Panning & Romanowicz 2006), but with predictions for depths of (a) 150 km, (b) 200 km, (c) 250 km and (d) 300 km. Predicted anisotropy directions are plotted on top of SKS splitting directions (red vectors: this study; purple vectors: compiled by Becker *et al*. 2012).

Figure S13. Same as Fig. S12, but for model SH11_TX2008 (Simmons *et al.* 2009; Schmandt & Humphreys 2010, 2011; Becker 2012).

Figure S14. Same as Fig. S12, but for model HMSL-p06 (Houser *et al*. 2008).

Figure S15. Same as Fig. S12, but for model SEMum (Lekić & Romanowicz 2011).

(http://gji.oxfordjournals.org/lookup/suppl/doi:10.1093/gji/ggw271/-/DC1).

Please note: Oxford University Press is not responsible for the content or functionality of any supporting materials supplied by the authors. Any queries (other than missing material) should be directed to the corresponding author for the paper.